ACS APPLIED MATERIALS & INTERFACES

Research Article

www.acsami.org

# New Energy Storage Option: Toward $ZnCo_2O_4$ Nanorods/Nickel Foam Architectures for High-Performance Supercapacitors

Bin Liu,[†,‡] Boyang Liu,[‡] Qiufan Wang,[‡] Xianfu Wang,[‡] Qingyi Xiang,[‡] Di Chen,*[,‡] and Guozhen Shen*[,†]

[†]State Key Laboratory for Superlattices and Microstructures, Institute of Semiconductors, Chinese Academy of Sciences, Beijing 100083, P. R. China.

[‡]Wuhan National Laboratory for Optoelectronics (WNLO) and College of Optical and Electronic Information, Huazhong University of Science and Technology (HUST), Wuhan 430074, P. R. China.

Supporting Information

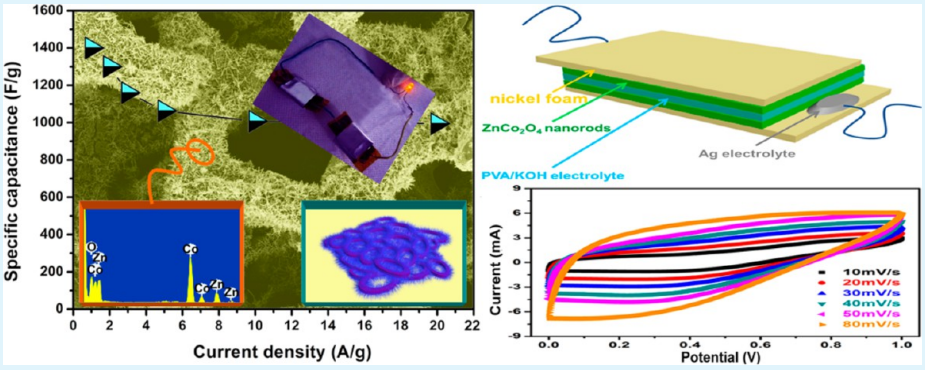


**ABSTRACT:** Hierarchical $ZnCo_2O_4$/nickel foam architectures were first fabricated from a simple scalable solution approach, exhibiting outstanding electrochemical performance in supercapacitors with high specific capacitance (~1400 F $g^{-1}$ at 1 A $g^{-1}$), excellent rate capability (72.5% capacity retention at 20 A $g^{-1}$), and good cycling stability (only 3% loss after 1000 cycles at 6 A $g^{-1}$). All-solid-state supercapacitors were also fabricated by assembling two pieces of the $ZnCo_2O_4$-based electrodes, showing superior performance in terms of high specific capacitance and long cycling stability. Our work confirms that the as-prepared architectures can not only be applied in high energy density fields, but also be used in high power density applications, such as electric vehicles, flexible electronics, and energy storage devices.

**KEYWORDS:** *energy storage, supercapacitors, $ZnCo_2O_4$/Ni foam architecture, high-performance, promising applications*

## 1. INTRODUCTION

High-performance, lightweight, and environmentally friendly energy storage devices, such as supercapacitors and lithium-ion batteries, are urgently needed for sustainable and renewable power sources in modern electronic industry.[1,2] Typically, Li-ion batteries have high energy densities, low power densities, and limited cycle lives.[3−9] On the contrary, with the features of higher power density than batteries, and higher energy density than conventional dielectric capacitors, supercapacitors have attracted much attention for next-generation power devices.[10−14]

Transition metal (Ni, Co, Ru, etc.) oxides and hydroxides have been investigated to be used as active materials for supercapacitors because they have theoretical specific capacitance (SC) values higher than 1000 F $g^{-1}$.[15−18] However, these is still plenty of room to enhance the most experimental capacitive values of these systems.[19−22] Studies found that electrodes with suitable porous or network microstructures can well enhance not only power density but also cycling stability for supercapacitors, which open new ways to develop high-performance supercapacitors.[23,24] Therefore, finding specific porous or network electrode materials with enhanced performance is highly desired.

$ZnCo_2O_4$ is a promising functional material that has been investigated for applications in Li-ion batteries, electrocatalysts, etc.[25−27] However, too little information about $ZnCo_2O_4$ materials as electrodes for high performance supercapacitors was disclosed till now.[2,28,29] Considering previous reports on the cobaltite-based electrodes, it reveals that $NiCo_2O_4$ and $ZnCo_2O_4$ electrodes evidently delivered superior capacitive performance because of their higher electrochemical activity, richer redox reactions than $Co_3O_4$.[2,15,30,31] Additionally, recent reports have demonstrated that one-dimensional $ZnCo_2O_4$ nanowires grown on the current collectors could achieve high-performance electrochemical properties for Li-ion batteries.[25,27] It is expected that the 1D $ZnCo_2O_4$ nanostructures/current collector composites serving as promising active materials may also have a superior capacitive performance

Received: June 17, 2013
Accepted: September 19, 2013
Published: September 19, 2013

  

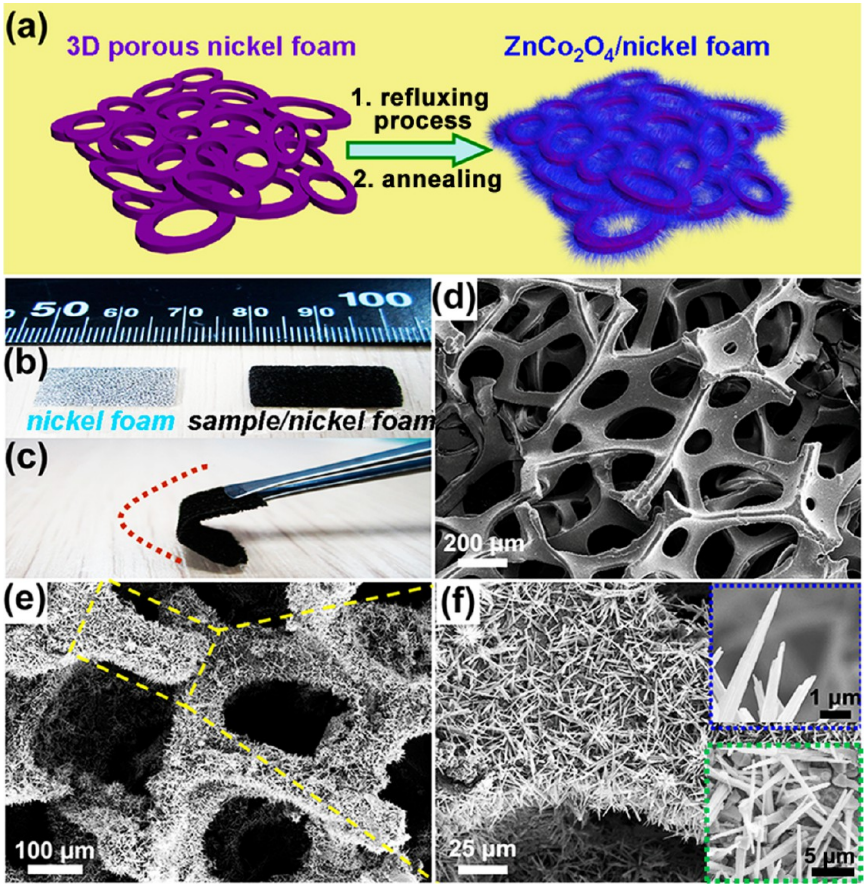


**Figure 1.** (a) Schematic representation of the $ZnCo_2O_4$ nanorods/nickel foam synthesis. (b, c) photographs of the obtained products without and with bending, (d) SEM image of the pristine nickel foam, and (e, f) the $ZnCo_2O_4$ nanorods grown on it.

compared to their binary oxide conterparts. Herein, we first report the fabrication of hierarchical $ZnCo_2O_4$ architectures on porous nickel foam via a polyol refluxing process followed by thermal treatment. Assembled as supercapacitors, the hierarchical nanostructured electrode showed good capacitive behavior with an enhanced SC of ~1400 F $g^{-1}$ at 1 A $g^{-1}$, excellent rate capacity (72.5% capacity retention at 20 A $g^{-1}$) and good cycling stability. To verify the great feasibility for the as-fabricated $ZnCo_2O_4$-based electrodes in a complete storage unit, we further assembled all-solid-state supercapacitors by using two pieces of these electrodes, which shows their superior performance and great promising power.

## 2. EXPERIMENTAL METHODS

**Preparation of Nickel Foam Substrate.** Before the fabrication of $ZnCo_2O_4$ samples, the nickel foam substrate was cleaned by sonication sequentially in acetone, deionized (DI) water, and ethanol for 30 min each. After being dried, the well-cleaned nickel foam was transferred into a flask.

**Synthesis of Hierarchical $ZnCo_2O_4$/Nickel Foam Architectures.** All the reagents were analytical grade and used without further purification. Hierarchicial $ZnCo_2O_4$/nickel foam architectures were fabricated from a simple polyol refluxing process, according to the previous similar procedures.[32] In a typical procedure, 0.5 mmol of $Zn(NO_3)_2 \bullet 6H_2O$ and 1 mmol of $Co(NO_3)_2 \cdot 6H_2O$ were first dispersed in 30 mL of deionized water. Sequently, the mixed solution was transferred into a 250 mL three-necked flask with cleaned nickel foam and heated to 80 °C. Then, 6 mmol of oxalic acid was dissolved in 20 mL of deionized water and then slowly injected into the flask. Under magnetic stirring, the reaction system was kept at 80 °C for 2 h and then cooled to room temperature naturally. After the flask cooled down to room temperature, the product was collected, washed, vacuum-dried, and then thermal treated at 400 °C for 2 h.

**Characterization.** X-ray diffraction patterns (XRD) were obtained from a X-ray diffractometer (X′ Pert PRO, PANalytical B.V., The Netherlands) with radiation of a Cu target (Ka, $\lambda$= 0.15406 nm). The morphologies and size-distributions of samples were characterized by field emission scanning electron microscopy (FESEM; JEOL JSM-6700F, 5 kV), and transmission electron microscopy (HRTEM; JEOL, JEM-2010 HT). A field-emission scanning electron microscope (Hitachi FE-SEM S4800) equipped with an Energy dispersive X-ray (EDX) analyzer was used to investigate the morphologies and compositions of the samples.

**Electrochemical Characterizations.** The electrochemical properties of $ZnCo_2O_4$/nickel foam products were carried out in a classical three electrodes setup: hierarchical $ZnCo_2O_4$/nickel foam architectures were directly used as working electrode; a platinum plate served as a counter electrode; and a Hg/HgO electrode served as a reference electrode. The cyclic voltammetry (CV) and galvanostatic charge/discharge of capacitors were investigated in 1 M KOH aqueous solution at a voltage window of 0−0.4 V on an electrochemical workstation (CHI 760D). Similarly, the all-solid-state SCs were fabricated by assembling two pieces of $ZnCo_2O_4$-based electrodes. PVA/KOH composite gel electrolyte was prepared by mixing PVA powder (6 g), KOH (6 g), and deionized water (60 mL) and then heating to 85 °C under vigorous stirring until the solution became homogeneous. The cyclic voltammetry (CV) and galvanostatic charge/discharge of devices were performed between 0 and 1.0 V at various current densities.

## 3. RESULTS AND DISCUSSION

The schematic of the 3D porous nickel foam substrate and hierarchical $ZnCo_2O_4$/nickel foam structures is shown in Figure

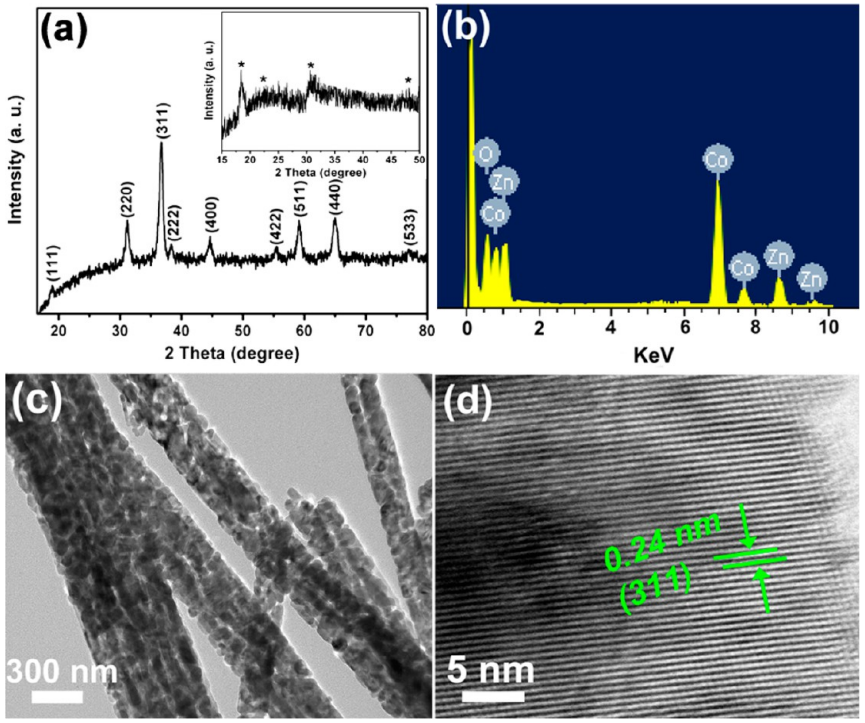


**Figure 2.** (a) XRD pattern, (b) EDS spectrum, (c) TEM image, and (d) HRTEM image of the as-obtained $ZnCo_2O_4$ nanorods. Inset: the XRD pattern of the precursors.

1a, showing aligned nanorods coated on nickel foam substrate after reaction. Briefly, in the refluxing process, the $Zn^{2+}$ and $Co^{2+}$ can react with $H_2C_2O_4$, acting as a key reagent, to synthesize $ZnCo_2(C_2O_4)_3$ precursors grown on Ni foam.[32] The above precursors were then transformed into the final $ZnCo_2O_4$ nanorods products/Ni foam composites due to the release of $CO_2$ and oxidation of $Co^{2+}$ into $Co^{3+}$ when further thermal-treatment process was fully completed. Photographs of the nickel foam before and after polyol refluxing synthesis are shown in Figure 1b and 1c, respectively. The obvious color change from metallic silver to black indicates the uniform deposition of $ZnCo_2O_4$ products on the large scale nickel foam. More importantly, the final hierarchical $ZnCo_2O_4$/nickel foam structures still preserve the excellent flexibility of the original nickel foam, which is benefical to fabricate wearable devices for flexible energy storage applications. Figure 1d depicts the SEM image of the pure nickel foam with network structures and smooth surfaces. After synthesis, high-density nanorods were found deposited on the whole foam, as can be seen in Figure 1e. A magnified SEM image of the selected area framed in Figure 1e is shown in Figure 1f, inset up and down of Figure 1f, and Figure S1 in the Supporting Information. It clearly reveals that the as-obtained $ZnCo_2O_4$ nanorods have uniform diameters of 300−500 nm (inset up) and lengths of 10 $\mu$m (inset down).

The phase and composition of the nanorods were investigated by peeling off the nickel foam and then using X-ray diffraction (XRD). In inset of Figure 2a, the XRD pattern of the precursor is well consistent with previous reports,[33,34] which can confirm that the precursor is $ZnCo_2(C_2O_4)_3{\cdot}6H_2O$. The corresponding XRD pattern of the annealed products is depicted in Figure 2a. All of the diffraction peaks can be readily indexed to pure cubic $ZnCo_2O_4$ phase (JCPDS Card No. 23−1390) without any detectable peaks from impurities. Peaks from Zn, Co and O elements were clearly observed form energy dispersive spectroscopy (EDS) spectrum of the as-prepared samples (Figure 2b). Moreover, the corresponding molar ratio of these elements from the EDS spectrum was demonstrated in Table S1 in the Supporting Information, showing that the molar ratio of Zn: Co: O is ∼1: 2: 4 within the samples. All these results further confirm the formation of $ZnCo_2O_4$ pure phase. The microstructures of the $ZnCo_2O_4$ nanorods were also investigated by using transmission electron microscopy (TEM). Figure 2c shows a low-magnification TEM image of several $ZnCo_2O_4$ nanorods. From the image we can see that the $ZnCo_2O_4$ nanorods are porous nanorods with diameters of about 300−500 nm, consisting with the SEM results. Figure 2d demonstrates the HRTEM image of a single porous $ZnCo_2O_4$ nanorod. The clearly resolved lattice fringes show an interplanar spacing of 0.24 nm, corresponding to the (311) planes of $ZnCo_2O_4$.

To evaluate the capacitive performance of the as-obtained hierarchical $ZnCo_2O_4$ nanorods/nickel foam, we carried out cycle voltammetry (CV) and galvanostatic charge−discharge measurements in a 1 M KOH aqueous solution using a three electrode system at room temperature (Figure 3a). Figure 3b shows the CV measurements of the hierarchical $ZnCo_2O_4$/nickel foam electrodes in the potential window of 0−0.4 V versus Hg/HgO at scan rates of 10, 30, 50, and 80 mV $s^{-1}$, respectively. From the curves, it can be seen that the redox peaks positions shifted with the increase of the scan rate from 10 to 80 mV $s^{-1}$. In addition, it can be observed that the specific capacitance of these electrodes decreases with the increase of scan rate ranging from 10 to 80 mV $s^{-1}$. This is attributed to the limited charge transfer and diffusion rate of electrolyte which is not fast enough to satisfy the electrochemical reactions of the electrode materials at high scan rates.[35−37] On the contrary, the capacity of electrodes may deliver the weak influence from ion transport at a low scan rate.[38] In Figure 3b, it is observed that pure nickel foam has an extremely small area

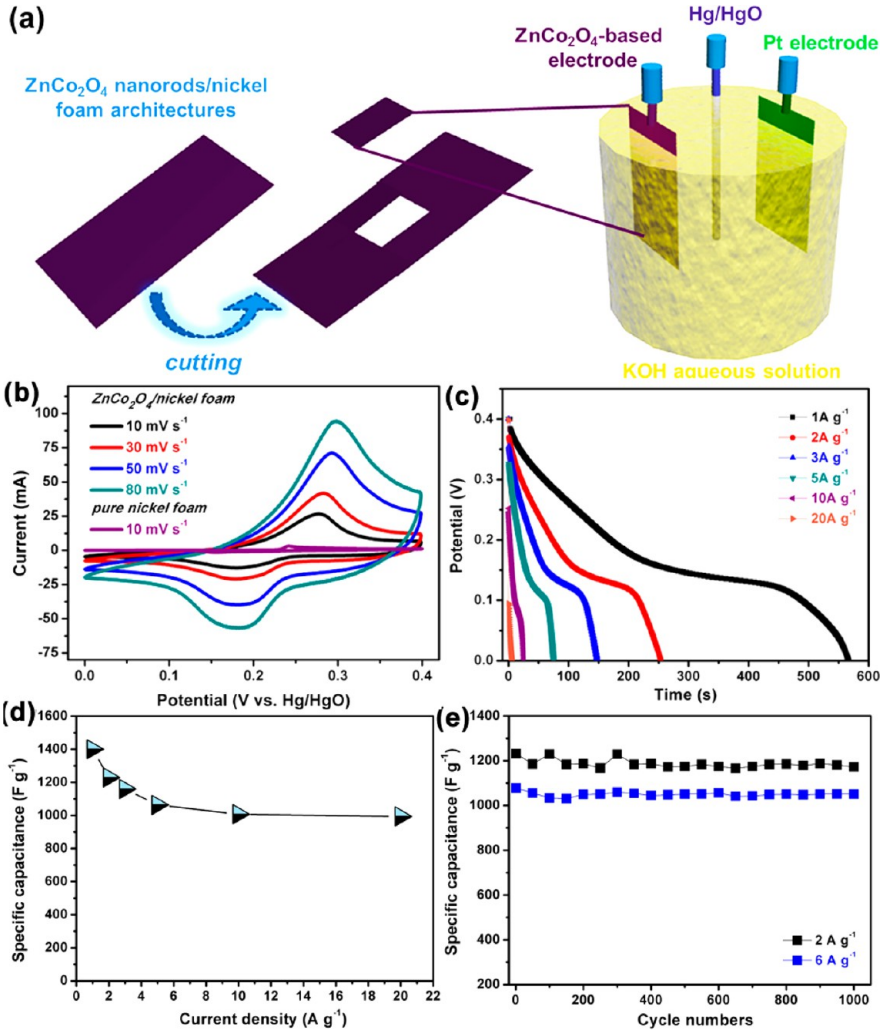


**Figure 3.** (a) Schematic of the fabrication process for the three-electrode measurement system. (b) CV curves of the $ZnCo_2O_4$ nanorods/nickel foam at the different scan rates. (c) Discharging curves at different current densities. (d) The specific capacitance as a function of the current densities of the $ZnCo_2O_4$ nanorods. (e) Cycling performance of the $ZnCo_2O_4$ nanorods/nickel foam electrodes at various current densities of 2 and 6 A g$^{-1}$.

surrounded by CV curves at 10 mV s$^{-1}$, suggesting that the capacitance contribution from the annealed Ni foam is negligible. Thus, the source of total capacitance arises primarily from the redox pseudocapacitance of the loaded $ZnCo_2O_4$. The pair of peaks is assigned to the $Co(OH)_2$/CoOOH redox couple prior to the onset of oxygen evolution, illustrates high redox reversibility for these electrodes. Also, the CV curves of the $ZnCo_2O_4$ presented here possess a much more uniform distribution of the enclosed area than those of $Co_3O_4$ electrodes reported previously, which reveals that ternary oxides like $ZnCo_2O_4$ in this case can be served as suitable active materials for supercapacitors due to the possible increase in feasible oxidation states.[30] Figure 3c presents the galvanostatic charge−discharge curves of the $ZnCo_2O_4$ nanorods based electrodes at different current densities ranging from 1 to 20 A g$^{-1}$ in the potential window of 0−0.4 V. The specific capacitance from discharge curves could be calculated from eq 1:

$$Csp = I\Delta t/m\Delta V \quad (1)$$

Where $I$ (mA) refers to the constant discharge current, $m$ (mg), $\Delta t$ (s), and $\Delta V$ (V) designate the mass of active material, discharge time, and potential drop during discharge.

The SC of the $ZnCo_2O_4$/nickel foam electrodes calculated from each discharge curve is about 1400, 1220, 1150, 1080, 1050, and 1015 F g$^{-1}$ at 1, 2, 3, 5, 10, and 20 A g$^{-1}$, respectively, as shown in Figure 3d. Most importantly, the specific capacitance of the $ZnCo_2O_4$-based electrodes remained almost constant within a variable range at high scan rates from 5 to 20 A g$^{-1}$. The Csp of the $ZnCo_2O_4$ based electrodes still keeps at 1015 F g$^{-1}$ when the current density was increased to 20 A g$^{-1}$, demonstrating their excellent rate capability. The results illustrated the high-capacity at a wide range of current densities, terrific rate capability, and high energy density of the present hierarchical $ZnCo_2O_4$/nickel foam structures. Figure 3e shows the cycling performance of the $ZnCo_2O_4$ nanorods based electrodes at two different current densities of 2 and 6 A g$^{-1}$, respectively. After 1000 charge−discharge cycles, the specific capacitances still keep at about 1180 and 1078 F g$^{-1}$, respectively, revealing very good reversibility with only about 3% loss at 6 A g$^{-1}$ after 1000 cycles. The corresponding charge−discharge curves of the first 5 cycles and the last 5

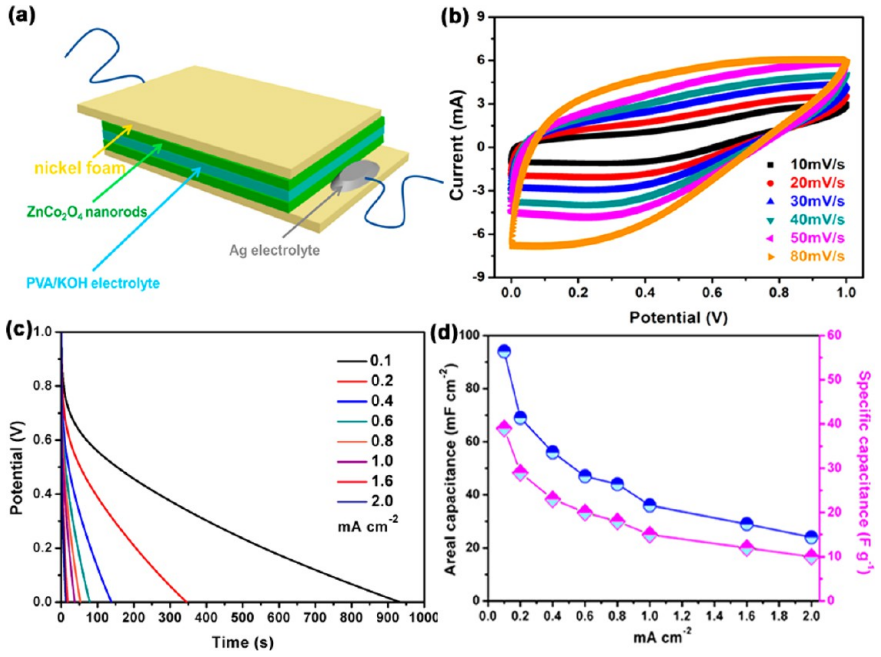


**Figure 4.** (a) Schematic illustration of the structure of the as-assembled all-solid-state devices. Electrochemical characterizations of these supercapacitors based on the $ZnCo_2O_4$/nickel foam electrodes in the voltage window of 0−1.0 V using a PVA/KOH electrolyte. (b) CV curves at various scan rates, (c) discharge curves at different current densities, (d) rate capability. Loading density of samples is approximately 1.2 mg cm$^{-2}$ for one electrode.

cycles were depicted in Figure S2a, b in the Supporting Information. From the curves, we can see that the curves did not show obvious differences, indicating that the $ZnCo_2O_4$/nickel foam electrodes showed excellent long-term electrochemical stability and good reversible redox behaviors.

The all-solid-state SC devices in terms of safety consideration are superior to their counterparts with liquid electrolytes including robust encapsulation to prevent leakage of liquid electrolyte and package units making them bulky. Herein, on the basis of the above electrodes using liquid electrolytes, we further assembled the all-solid-state devices based on two composite electrodes, which consist of two (sandwiched construction: the as-synthesized $ZnCo_2O_4$−Ni foams/PVA-based solid electrolyte/$ZnCo_2O_4$−Ni foam), as shown in Figure 4 and Figure S3 in the Supporting Information. Figure 4b shows the rectangular-like shape in CV curves of the electrodes between 0 and 1.0 V at various current densities of 10, 20, 30, 40, 50, and 80 mV s$^{-1}$, respectively, revealing the composite electrodes are mainly described as a double-layer behavior.[28] Thus, the capacitance arises from unique hierarchical $ZnCo_2O_4$/nickel foam networks for storing electrical charge. From the plot, it can be observed that the curves of the two-electrode systems are obviously different with those of the above three-electrode systems, which mainly represent the absence of redox peaks. Briefly, supercapacitors can be classified into two categories: the non-Faradic electrical double-layer capacitor and Faradaic redox pseudocapacitor. These two mechanisms can work separately or together, depending on the active electrode materials used in the capacitors. For our 2-electrode system, it clearly reveals that the feature of electrical double-layer capacitor occupied dominant position than that of typical pseudocapacitor. Besides, no obvious redox peaks are observed in the present work, indicating that the current supercapacitors are charged and discharged at a pseudoconstant rate.[23,39] Thus, we can get the conclusion that the two-electrode devices are primarily nonfaradaic within their corresponding voltage window.[28] Actually, this common phenomenon is observed in many symmetric supercapacitors reported previously.[2,15,28,31,40] Figure 4c further shows the discharge curves at various current densities. The calculated results of the specific capacity are illustrated in Figure 4d. The corresponding areal capacitance was calculated using eq 2

$$Ca = I\Delta t/s\Delta V \tag{2}$$

Where $I$ (mA) refers to the constant discharge current, $s$ (cm$^2$), $\Delta t$ (s), and $\Delta V$ (V) designate area of active material, discharge time, and potential drop during discharge. Loading density of samples is approximately 1.2 mg cm$^{-2}$ for one electrode. The devices based on the $ZnCo_2O_4$ nanorods/nickel foam electrodes exhibit enhanced capacitances of 94, 69, 56, 47, 44, 36, 29, and 24 mF cm$^{-2}$ (39, 29, 23, 20, 18, 15, 12, and 10 F g$^{-1}$ for a device) at the discharge currents of 0.1, 0.2, 0.4, 0.6, 0.8, 1.0, 1.6, and 2.0 mA cm$^{-2}$, respectively, showing their corresponding improved rate-performance. It is a common phenomenon that three-electrode system can achieve higher capacity value than two-electrode system due to the capacitance values of the $ZnCo_2O_4$ electrodes strongly depending on the cell configuration used for the electrochemical investigation, being always significantly higher for a three-electrode system.[41−43] In addition, the capacitance value for two-electrode systems will depend on the equilibrium potentials of both positive/negative electrodes. Especially with increasing the operating voltage of the capacitor, the potential of the positive electrode is mainly shifted in the positive direction, which leads to a smaller capacitance presented.[42] Although the specific capacity of our two-electrode supercapacitors is lower than the three-electrode ones, the binder-free two-electrode cells with better availability and incomparable merits should be evaluated in real capacitors, such as higher safety (not liquid leakage), better portability (desired assembly design), and more improved capacity.

Figure 5a shows the cycling performance of the devices that was performed at a current density of 0.5 mA $cm^{-2}$ for as long as 1400 cycles. The capacity retention of the as-assembled all-solid-state device remains approximately 100%, revealing its corresponding excellent cycling capability. From the plot, it can be seen that the capacitance loss after 1400 cycles is only 2.6%, as further evident from the very stable charge−discharge curves for the first and last 8 cycles in panels b and c in Figure 5, respectively. From the curves, we can see that the curves did not show obvious differences, further indicating that the $ZnCo_2O_4$/nickel foam devices showed the excellent long-term electrochemical stability.

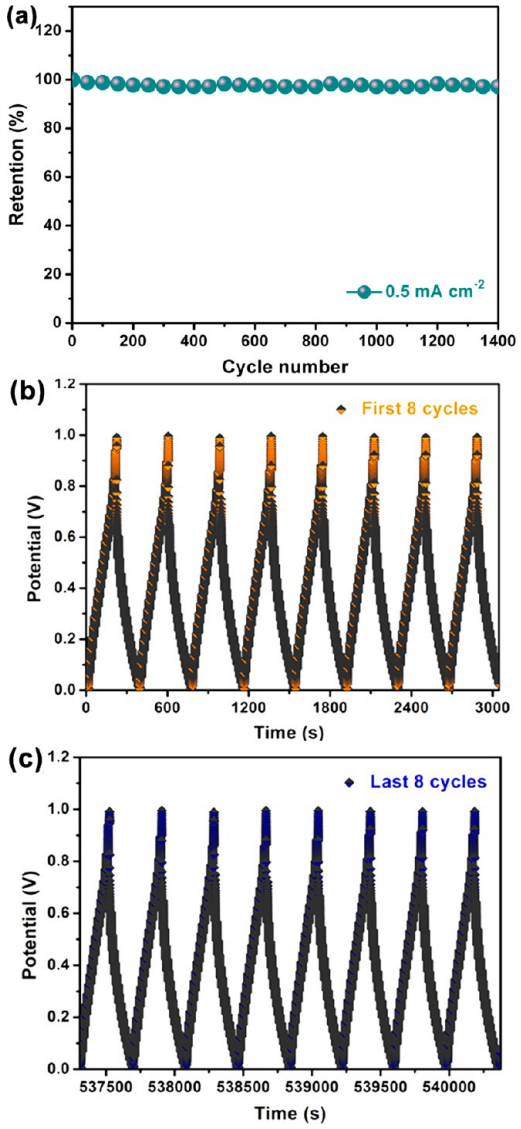


**Figure 5.** (a) Cycling performance of these as-assembled $ZnCo_2O_4$/nickel foam electrodes for 1400 cycles at 0.5 mA $cm^{-2}$. The corresponding charge−discharge curves of the (b) first and (c) last eight cycles.

All excellent performances of novel $ZnCo_2O_4$/nickel foam electrodes are also comparable to previous reported values of other $ZnCo_2O_4$ electrodes, as shown in Table S2 in the Supporting Information. On the premise of superior comprehensive features of our as-fabricated devices, they may be described as more potential candidates in supercapacitor applications. The greatly enhanced capacity, excellent rate capability, and cycling stability of the $ZnCo_2O_4$ nanorod-based electrodes may be attributed to the unique hierarchical porous electrode structures and the 1D shape. With the porous nickel foam as the skeleton, the as-obtained hierarchical structures have an outstanding electronic conductivity because the 1D $ZnCo_2O_4$ active material sticked tightly to the nickel foam, achieving excellent adhesion and electrical contact. It builds up an express way for charge transfer. Besides, the hierarchical 3D configuration of the porous $ZnCo_2O_4$ nanorods/nickel foam ensures the large surface area, loose textures and open spaces between neighboring nanorods, thus greatly increases the contact areas between electrolyte and the $ZnCo_2O_4$ nanorods, which improves electron/ion transport, enhances the kinetics of redox reactions, and facilitates facile stress relaxation during cycling.

As efficient and powerful energy storage devices, the SCs could, in principle, be charged and then discharged to drive various electronic units. To demonstrate the practical application of the as-assembled supercapacitors, the photo of two pieces of the as-fabricated supercapacitors after charged were connected in series and then they were connected with a yellow LED. Figure 6 and Figure S4 in the Supporting Information show the corresponding photograph of the assembled system. The yellow LED was successfully lightened by the supercapacitors, charged as-assembled SCs connected in series. From the plot, it can be seen that a yellow LED is lighted by two charged all-solid-state SCs in series, suggesting that these devices are very promising candidates for various practical applications.

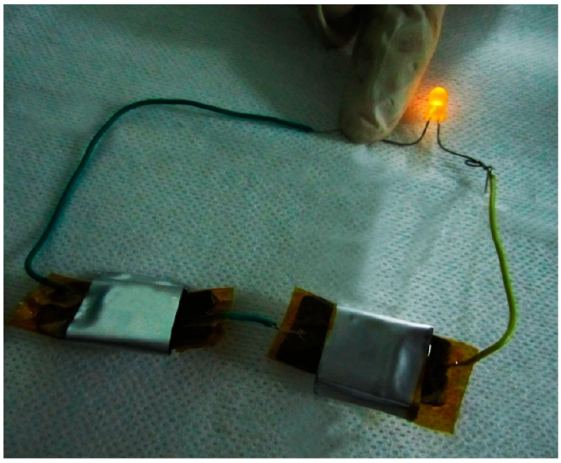

**Figure 6.** Optical image of a yellow LED powered by two charged all-solid-state SCs connected in series.

## 4. CONCLUSION

In summary, high-performance supercapacitor based on hierarchical $ZnCo_2O_4$ nanorods/nickel foam architecture has been successfully fabricated, exhibiting a very high specific capacitance of 1400 F $g^{-1}$ at 1A $g^{-1}$, enhanced rate capability and cycling stability (97% retention after 1000 cycles at 6 A $g^{-1}$). All-solid-state supercapacitors with superior electrochemical performances were successfully fabricated by assembling two pieces of the $ZnCo_2O_4$-based electrodes. Our results indicate that the $ZnCo_2O_4$ nanonods structure are highly desirable in the application of advanced electrochemical

electrode materials, also open up the opportunities for the devices configuration for flexible electronics, high energy storage devices, etc.

## ■ ASSOCIATED CONTENT

### Supporting Information

Typical SEM images, corresponding EDS microanalysis, charge−discharge curves of the first and last five cycles for hierarchical $ZnCo_2O_4$ nanorod/nickel foam, and optical image of the as-assembled all-solid-state $ZnCo_2O_4$/nickel foam devices. A comparison of the desired performance between existing $ZnCo_2O_4$/nickel foam composite electrodes and other reported electrodes. This material is available free of charge via the Internet at http://pubs.acs.org.

## ■ AUTHOR INFORMATION

### Corresponding Authors

*E-mail: gzshen@semi.ac.cn.
*E-mail: dichen@mail.hust.edu.cn.

### Notes

The authors declare no competing financial interest.

## ■ ACKNOWLEDGMENTS

This work was supported by the National Natural Science Foundation (21001046, 61377033, 91123008, 51002059), the 973 Program of China (2011CB933300), and the Program for New Century Excellent Talents of the University in China (Grant NCET-11-0179). Special thanks to the Analytical and Testing Center of HUST and the Center of Micro-Fabrication and Characterization (CMFC) of WNLO for using their facilities.

## ■ REFERENCES

(1) Chen, T.; Qiu, L.; Yang, Z.; Cai, Z.; Ren, J.; Li, H.; Lin, H.; Sun, X.; Peng, H. *Angew. Chem., Int. Ed.* **2012**, *51*, 11977−11980.
(2) Liu, B.; Tan, D. S.; Wang, X. F.; Chen, D.; Shen, G. Z. *Small* **2013**, *9*, 1998−2004.
(3) Liu, B.; Wang, X. F.; Chen, H. T.; Wang, Z. R.; Chen, D.; Cheng, Y. B.; Zhou, C. W.; Shen, G. Z. *Sci. Rep.* **2013**, *3*, 1622.
(4) Ding, S. J.; Chen, J. S.; Qi, G. G.; Duan, X. N.; Wang, Z. Y.; Giannelis, E. P.; Archer, L. A.; Lou, X. W. *J. Am. Chem. Soc.* **2011**, *133*, 21−23.
(5) Seo, M. H.; Park, M.; Lee, K. T.; Kim, K.; Kimb, J.; Cho, J. *Energy Environ. Sci.* **2011**, *4*, 425−428.
(6) Hertzberg, B.; Alexeev, A.; Yushin, G. *J. Am. Chem. Soc.* **2010**, *132*, 8548−8549.
(7) Qu, B. H.; Zhang, M.; Lei, D. N.; Zeng, Y. P.; Chen, Y. J.; Chen, L. B.; Li, Q. H.; Wang, Y. G.; Wang, T. H. *Nanoscale* **2011**, *3*, 3646−3651.
(8) Jiang, J.; Li, Y. Y.; Liu, J. P.; Huang, X. T.; Yuan, C. Z.; Lou, X. W. *Adv. Mater.* **2012**, *24*, 5166−5180.
(9) Zhang, C. F.; Wu, H. B.; Yuan, C. Z.; Guo, Z. P.; Lou, X. W. *Angew. Chem., Int. Ed.* **2012**, *51*, 9592−9595.
(10) Fan, Z. J.; Yan, J.; Wei, T.; Zhi, L. J.; Ning, G. Q.; Li, T. Y.; Wei, F. *Adv. Funct. Mater.* **2011**, *21*, 2366−2375.
(11) Liu, J. P.; Jiang, J.; Cheng, C. W.; Li, H. X.; Zhang, J. X.; Gong, H.; Fan, H. J. *Adv. Mater.* **2011**, *23*, 2076−2079.
(12) Wang, Z. Y.; Luan, D. Y.; Madhavi, S.; Li, C. M.; Lou, X. W. *Chem. Commun.* **2011**, *47*, 8061−8063.
(13) Chen, P. C.; Shen, G. Z.; Shi, Y.; Chen, H. T.; Zhou, C. W. *ACS Nano* **2010**, *4*, 4403−4411.
(14) Jiang, H.; Li, C. Z.; Sun, T.; Ma, J. *Chem. Commun.* **2012**, *48*, 2606−2608.
(15) Wang, Q. F.; Wang, X. F.; Liu, B.; Yu, G.; Hou, X. J.; Chen, D.; Shen, G. Z. *J. Mater. Chem. A* **2013**, *1*, 2468−2473.
(16) Chen, P. C.; Chen, H. T.; Qiu, J.; Zhou, C. W. *Nano Res.* **2010**, *3*, 594−603.
(17) Wang, B.; Zhu, T.; Wu, H. B.; Xu, R.; Chen, J. S.; Lou, X. W. *Nanoscale* **2012**, *4*, 2145−2149.
(18) Zhu, T.; Chen, J. S.; Lou, X. W. *J. Mater. Chem.* **2010**, *20*, 7015−7020.
(19) Yu, G. H.; Hu, L. B.; Liu, N.; Wang, H. L.; Vosgueritchian, M.; Yang, Y.; Cui, Y.; Bao, Z. *Nano Lett.* **2011**, *11*, 4438−4442.
(20) Wang, X.; Sumboja, A.; Khoo, E.; Yan, C.; Lee, P. S. *J. Phys. Chem. C* **2012**, *116*, 4930−4935.
(21) Liu, J. P.; Cheng, C. W.; Zhou, W. W.; Li, H. X.; Fan, H. J. *Chem. Commun.* **2011**, *47*, 3436−3438.
(22) Kotz, R.; Carlen, M. *Electrochim. Acta* **2000**, *45*, 2483−2498.
(23) Yang, L.; Cheng, S.; Ding, Y.; Zhu, X. B.; Wang, Z. L.; Liu, M. L. *Nano Lett.* **2012**, *12*, 321−325.
(24) Simon, P.; Gogotsi, Y. *Nat. Mater.* **2008**, *7*, 845−854.
(25) Liu, B.; Wang, X. F.; Liu, B. Y.; Wang, Q. F.; Tan, D. S.; Song, W. F.; Hou, X. J.; Chen, D.; Shen, G. Z. *Nano Res.* **2013**, *6*, 525−534.
(26) Lin, C.; Li, Y. Y.; Yu, M.; Yang, P. P.; Lin, J. *Adv. Funct. Mater.* **2007**, *17*, 1459−1465.
(27) Liu, B.; Zhang, J.; Wang, X. F.; Chen, G.; Chen, D.; Zhou, C. W.; Shen, G. Z. *Nano Lett.* **2012**, *12*, 3005−3011.
(28) Karthikeyan, K.; Kalpana, D.; Renganathan, N. G. *Ionics* **2009**, *15*, 107−110.
(29) Davis, M.; Gumeci, C.; Black, B.; Korzeniewski, C.; Hope-Weeks, L. *RSC Adv.* **2012**, *2*, 2061−2066.
(30) Wei, T. Y.; Chen, C. H.; Chien, H. C.; Lu, S. Y.; Hu, C. C. *Adv. Mater.* **2010**, *22*, 347−351.
(31) Lu, X. H.; Huang, X.; Xie, S. L.; Zhai, T.; Wang, C. S.; Zhang, P.; Yu, M. H.; Li, W.; Liang, C. L.; Tong, Y. X. *J. Mater. Chem.* **2012**, *22*, 13357−13364.
(32) Du, N.; Xu, Y. F.; Zhang, H.; Yu, J. X.; Zhai, C. X.; Yang, D. R. *Inorg. Chem.* **2011**, *50*, 3320−3324.
(33) Song, F. L.; Huang, L. R.; Chen, D. H.; Tang, W. J. *Mater. Lett.* **2008**, *62*, 543−547.
(34) Bazuev, G. V.; Gyrdasova, O. I.; Grigorov, I. G.; Koryakova, O. V. *Inorg. Mater.* **2005**, *41*, 288−292.
(35) Liu, W. W.; Yan, X. B.; Lang, J. W.; Peng, C.; Xue, Q. J. *J. Mater. Chem.* **2012**, *22*, 17245−17253.
(36) Wang, Q. F.; Liu, B.; Wang, X. F.; Ran, S. H.; Wang, L. M.; Chen, D.; Shen, G. Z. *J. Mater. Chem.* **2012**, *22*, 21647−21653.
(37) Hu, L. B.; Chen, W.; Xie, X.; Liu, N.; Yang, Y.; Wu, H.; Yao, Y.; Pasta, M.; Alshareef, H. N.; Cui, Y. *ACS Nano* **2011**, *5*, 8904−8913.
(38) Weng, Z.; Su, Y.; Wang, D. W.; Li, F.; Du, J. H.; Cheng, H. M. *Adv. Energy Mater.* **2011**, *1*, 917−922.
(39) Lang, X. Y.; Hirata, A.; Fujita, T.; Chen, M. W. *Nat. Nanotechnol.* **2011**, *6*, 232−236.
(40) Horng, Y. Y.; Lu, Y. C.; Hsu, Y. K.; Chen, C. C.; Chen, L. C.; Chen, K. H. *J. Power Sources* **2010**, *195*, 4418−4422.
(41) Cheng, Q.; Tang, J.; Ma, J.; Zhang, H.; Shinya, N.; Qin, L. C. *Phys. Chem. Chem. Phys.* **2011**, *13*, 17615−17624.
(42) Khomenko, V.; Frackowiak, E.; Beguin, F. *Electrochim. Acta* **2005**, *50*, 2499−2506.
(43) Frackowiak, E.; Khomenko, V.; Jurewicz, K.; Lota, K.; Beguin, F. *J. Power Sources* **2006**, *153*, 413−418.